Changes in the MJO under Greenhouse Gas–Induced Warming in CMIP5 Models

STEPHANIE S. RUSHLEY AND DAEHYUN KIM

Department of Atmospheric Sciences, University of Washington, Seattle, Washington

ÁNGEL F. ADAMES

Department of Climate and Space Science and Engineering, University of Michigan, Ann Arbor, Michigan

(Manuscript received 5 July 2018, in final form 19 November 2018)

ABSTRACT

This study investigates changes to the Madden–Julian oscillation (MJO) in response to greenhouse gas–induced warming during the twenty-first century. Changes in the MJO's amplitude, phase speed, and zonal scale are examined in five models from phase 5 of the Coupled Model Intercomparison Project (CMIP5) that demonstrate superior MJO characteristics. Under warming, the CMIP5 models exhibit a robust increase in the spectral power of planetary-scale, intraseasonal, eastward-propagating (MJO) precipitation anomalies (~10.9% K^{-1}). The amplification of MJO variability is accompanied by an increase of the spectral power of the corresponding westward-traveling waves at a similar rate. This suggests that enhanced MJO variability in a warmer climate is likely caused by enhanced background tropical precipitation variability, not by changes in the MJO's stability. All models examined show an increase in the MJO's phase speed (1.8% K^{-1}–4.5% K^{-1}) and a decrease in the MJO's zonal wavenumber (1.0% K^{-1}–3.8% K^{-1}). Using a linear moisture mode framework, this study tests the theory-predicted phase speed changes against the simulated phase speed changes. It is found that the MJO's acceleration in a warmer climate is a result of enhanced horizontal moisture advection by the steepening of the mean meridional moisture gradient and the decrease in zonal wavenumber, which is partially offset by the lengthening of the convective moisture adjustment time scale and the increase in gross dry stability. While the ability of the linear moisture mode framework to explain MJO phase speed changes is model dependent, the theory can accurately predict the phase speed changes in the model ensemble.

1. Introduction

The Madden–Julian oscillation (MJO; Madden and Julian 1972) is a convectively coupled, planetary-scale disturbance that dominates tropical atmospheric variability in the intraseasonal time scale (30–90 days). The MJO's enhanced precipitation signal typically initiates within the Indo-Pacific warm pool (60°–180°E; Zhang and Ling 2017), propagates eastward at approximately 5 m s^{-1}, and dissipates in the central Pacific as it encounters cooler sea surface temperatures (SSTs; Milliff and Madden 1996; Matthews 2000). Circulation anomalies associated with the MJO can continue their eastward propagation beyond the central Pacific, circumnavigating the globe, and occasionally contribute to the initiation of new MJO events over the Indian Ocean (Madden and Julian 1972; Matthews 2008; Haertel et al. 2015; Powell and Houze 2015).

The MJO's effects are felt globally in the weather–climate system (Zhang 2013). Tropical cyclones have been shown to be 4 times more likely to occur in the eastern Pacific, Gulf of Mexico, and Caribbean Sea when the convective center of the MJO is located over the Indian Ocean and the low-level winds in the eastern Pacific are westerly (Maloney and Hartmann 2000a,b). The eastward propagation of the MJO over the Indian Ocean can influence the onset of the Asian and Australian monsoons (Risbey et al. 2009; Wheeler et al. 2009; Marshall and Hendon 2015). Westerly wind bursts associated with the MJO can trigger Kelvin waves in the Pacific Ocean, which can lead to an initiation of positive-phase El Niño–Southern Oscillation (ENSO) events (e.g., Hendon et al. 1999; Pohl and Matthew 2007; Marshall et al. 2009). In addition to direct impacts on

Supplemental information related to this paper is available at the Journals Online website: https://doi.org/10.1175/JCLI-D-18-0437.s1.

Corresponding author: Daehyun Kim, daehyun@uw.edu

DOI: 10.1175/JCLI-D-18-0437.1

© 2019 American Meteorological Society. For information regarding reuse of this content and general copyright information, consult the AMS Copyright Policy (www.ametsoc.org/PUBSReuseLicenses).

Brought to you by NOAA Central Library | Unauthenticated | Downloaded 02/28/22 06:29 PM UTC

tropical cyclogenesis, monsoon onset, and ENSO, the MJO has wide-reaching teleconnections via Rossby wave trains that propagate to the extratropics and affect the weather in the midlatitudes (e.g., Kim et al. 2006; Lin et al. 2006; Cassou 2008). Given the extensive impacts of the MJO, understanding changes to the MJO under greenhouse gas–induced warming may lend insight into how other aspects of the weather–climate system will change.

Previous studies that have examined the effects of greenhouse gas–induced warming on the MJO found that the amplitude of MJO precipitation variance increases with warming (Subramanian et al. 2014; Schubert et al. 2013; Maloney and Xie 2013; Arnold et al. 2013, 2015; Adames et al. 2017a; Wolding et al. 2017; Bui and Maloney 2018). For example, Subramanian et al. (2014) found that intraseasonal precipitation variance increases with increasing surface temperatures in Community Climate System Model, version 4 (CCSM4), while Schubert et al. (2013) found an increase in the MJO amplitude under a CO_2-driven warming in the Max Planck Institute Earth System Model (MPI-ESM). While reporting a similar result—MJO amplification with warming—in the National Aeronautics and Space Administration (NASA) Goddard Institute for Space Studies (GISS) model, Adames et al. (2017a) also showed that intraseasonal, planetary-scale, westward-propagating waves amplify at nearly the same rate as the MJO. They speculated that the amplification of the MJO could be due to changes in tropical precipitation variance and not due to destabilization of the MJO with warming. Interestingly, the increase in the MJO wind variance with warming is found to be smaller than that in the MJO precipitation variance in model simulations because of an increase in the tropical dry static stability (Maloney and Xie 2013; Adames et al. 2017a; Bui and Maloney 2018). Some models that show an increase in the MJO precipitation variance even show a decrease in the MJO zonal wind variance (Bui and Maloney 2018).

Further, numerous modeling studies have shown a robust increase in the phase speed of the MJO (Arnold et al. 2013, 2015; Chang et al. 2015; Adames et al. 2017a; Haertel 2018). The increase in the phase speed coincides with an increase in the frequency of the MJO (Slingo et al. 1999; Arnold et al. 2013; Chang et al. 2015). Arnold et al. (2013) showed a shift of the MJO peak in the power spectrum of outgoing longwave radiation (OLR) toward higher frequencies when SST was increased in the superparameterized Community Atmosphere Model (SP-CAM). Chang et al. (2015) also reported an increase in the frequency of the MJO spectral power in the European Centre Hamburg Model, version 5, Snow–Ice–Thermocline (ECHAM5-SIT) model in the representative concentration pathway (RCP) 8.5 simulation.

Although the modeling studies mentioned above are insightful, they are limited in that they used a single model and that they used different warming scenarios to simulate how the MJO responds to warming (Schubert et al. 2013; Arnold et al. 2015; Adames et al. 2017a,b; Maloney and Xie 2013; Arnold et al. 2013; Subramanian et al. 2014; Chang et al. 2015). A more complete analysis requires the analysis of a multimodel ensemble simulation performed under a uniform simulation setup. One of the goals of this study is to obtain a more robust understanding of how the MJO responds to greenhouse gas–induced warming by examining five models from phase 5 of the Coupled Model Intercomparison Project (CMIP5) that simulate a reasonable MJO. Also, while the changes in the MJO amplitude and phase speed with warming have been documented in many of the aforementioned studies, limited efforts have been made to explain the changes in a quantitative manner. Understanding the MJO's amplitude and phase speed changes with warming using the linear moisture mode framework proposed by Adames and Kim (2016) is another goal of the current study.

In the moisture mode theory, moisture is a prognostic variable and its evolution determines the evolution of the anomalous precipitation (Fuchs and Raymond 2005, 2007; Raymond and Fuchs 2009; Sugiyama 2009; Sobel and Maloney 2012, 2013; Adames and Kim 2016). From the perspective of moisture mode theory, the circulation anomalies associated with the MJO [i.e., the Kelvin and Rossby wave responses of a Matsuno–Gill response to a dipole of diabatic heating and cooling along the equator (Matsuno 1966; Gill 1980)] redistribute anomalous moisture such that there is enhanced moistening (drying) to the east (west) of the enhanced convection. This moisture tendency, largely due to moisture advection, induces eastward propagation (Maloney et al. 2010; Pritchard and Bretherton 2014; Kim et al. 2014; Adames and Wallace 2015; Wolding and Maloney 2015, among others).

Recently, Adames et al. (2017b) used the linear moisture mode framework proposed by Adames and Kim (2016) to explain the warming-induced changes in MJO propagation documented in the NASA GISS model. They found that moisture mode theory can quantitatively explain the increase of the MJO's phase speed with CO_2-induced warming, albeit with considerable uncertainty. The simulated percentagewise increase in the phase speed with surface warming can be explained by an increase in the moisture gradient and decrease in the zonal wavenumber, which is offset by an increase to both the gross dry stability and convective moisture adjustment time scale (Adames et al. 2017b). The combined contribution of these four fields results

Brought to you by NOAA Central Library | Unauthenticated | Downloaded 02/28/22 06:29 PM UTC

in a change to the advection of moisture by the horizontal winds, which leads to an acceleration of MJO propagation of ~3.5% K^{-1} in the NASA GISS model (see section 4 for specific mechanisms).

In our study, the moisture mode framework will be used to interpret how the MJO responds to warming in the CMIP5 models. It will be shown that the fields identified by Adames et al. (2017b) to explain the MJO's acceleration with warming in the NASA GISS model also explain changes in MJO propagation in the five CMIP5 models analyzed here.

This study is structured as follows. Data and methods are described in section 2. Changes to the MJO structure and propagation in the CMIP5 models will be shown in section 3. A brief review of the moisture mode framework and the potential of this theory to be used to understand how the MJO responds to changes in greenhouse gases is shown in section 4. The moisture mode framework is used to interpret MJO changes in the CMIP5 models in section 5. A summary and conclusions can be found in section 6.

2. Data and methods

a. Observations

Satellite-based observations of precipitation from the Global Precipitation Climatology Project (GPCP) from 1997 to 2012 (Huffman et al. 2001) and the Special Sensor Microwave Imager (SSM/I) version 7 product (Hilburn and Wentz 2008; Wentz et al. 2012) from 1998 to 2016 are used. GPCP precipitation is used to calculate power spectra of equatorial precipitation and to estimate the phase speed of the MJO. The simultaneous observations of precipitation and column-integrated specific humidity $\langle q \rangle$ from the SSM/I version 7 product are used in the calculation of the observed convective moisture adjustment time scale τ_c, following Rushley et al. (2018). Temperature data are obtained from the European Centre for Medium-Range Forecasts (ECMWF) interim reanalysis (ERA-Interim) four times daily from 1998 to 2016 (Dee et al. 2011). The ERA-Interim data have a horizontal resolution of 1.5° × 1.5° and we make use of the 29 vertical pressure levels that lie within the troposphere (100–1000 hPa).

b. CMIP5 simulations

Daily averaged precipitation, temperature, and specific humidity q for 95 years of the RCP8.5 simulations are obtained from the CMIP5 archive (Taylor et al. 2012). The RCP8.5 scenario is a business-as-usual scenario from the Intergovernmental Panel on Climate Change (IPCC), where the radiative forcing reaches 8.5 W m^{-2} by 2100 (Taylor et al. 2012). The observations and model data have been interpolated onto a 2.5° × 2.5° horizontal grid and restricted to the tropical latitude band between 30°N and 30°S.

c. Metrics for MJO characteristics

We obtain MJO amplitude, phase speed, and zonal wavenumber from the wavenumber–frequency power spectrum of 20–100-day bandpass-filtered equatorial (10°S–10°N) precipitation. The raw spectrum is calculated using 192-day segments that overlap by 96 days, each window is detrended, and a 15-day cosine taper is applied to either end of the time window. The wavenumber–frequency power spectrum (e.g., Hayashi 1971) of each segment is calculated and the resulting spectra are averaged. The amplitude of the MJO (east power) is defined as the sum of spectral power over the MJO band (defined here as eastward wavenumbers 1–6 and periods 20–100 days). We also define the east-to-west ratio (EWR) as the ratio of east power to its westward-moving counterpart of the same temporal and spatial scale (west power). We examine the changes in the EWR to determine the uniqueness of MJO amplitude changes relative to waves of similar scale.

The MJO's phase speed and zonal wavenumber are calculated as the power-weighted mean phase speed and zonal wavenumber over the MJO band. When applied to observations, this method yields a mean phase speed of about 6.5 m s^{-1}, a value that is consistent with that of previous studies of the observed MJO (Adames and Kim 2016; Kerns and Chen 2016; Zhang and Ling 2017). Using this method, a zonal wavenumber k of 2.7 is obtained for the observed MJO convective signal, which is consistent with the known horizontal scale of the MJO (Wheeler and Kiladis 1999). Note that we employ the power-spectrum-based method of estimating the phase speed and zonal wavenumber of the MJO instead of the lag-regression-based method used in previous studies (Adames et al. 2017a; Chang et al. 2015; Arnold et al. 2013, 2015). The changes in the phase speed using the power-spectrum-based method are consistently smaller than those found with the lag-regression-based method, but the power-spectrum-based method shows a more linear response to warming. We find that the power-spectrum-based method is more reliable than the lag-regression-based method, which can change significantly when parameters are changed (i.e., longitudinal extent over which the phase speed is calculated).

In the following section, the changes in the characteristics of the MJO are examined as the percentage difference between the later three 20-yr periods in the RCP8.5 simulation (2041–60, 2061–80, and 2081–2100) and an earlier 20-yr period of RCP8.5 (2021–40). For

Brought to you by NOAA Central Library | Unauthenticated | Downloaded 02/28/22 06:29 PM UTC

simplicity, we will refer to the period from 2021 to 2040 as the reference period. In most models, the linear changes within the RCP8.5 period cannot be linearly extrapolated to the historical or preindustrial simulation, presumably because of the effects of aerosol concentration or other changes that affect the mean state.

d. Model selection

We apply a set of criteria to all models available in the CMIP5 archive to ensure that only those that simulate a good MJO are used. Specifically, models that fail to satisfy the following conditions are excluded:

(i) The MJO signal in the wavenumber–frequency spectrum (e.g., a Wheeler–Kiladis diagram) shows a distinct peak in the MJO band that is separated from that of the convectively coupled Kelvin wave, as in observations (Fig. 1)
(ii) The lag-regression diagram of precipitation (Fig. 2) shows a continuous eastward propagation from the Indian Ocean to the west Pacific
(iii) EWR is comparable to or larger than the observed value in the reference period and remains greater than 1 for the duration of the RCP8.5 simulation (Fig. 3)
(iv) The average phase speed of the MJO in RCP8.5 simulation is larger than $3\,\mathrm{m\,s^{-1}}$ (Table 1). This last condition is based on the fact that the observed phase speed of the MJO rarely falls below $3\,\mathrm{m\,s^{-1}}$ (Kerns and Chen 2016; Zhang and Ling 2017)

Five models remain after this selection process: CMCC-CM, CMCC-CMS, CNRM-CM5, IPSL-CM5B-LR, and MRI-CGCM3. Table 1 lists the models used in this study, along with the MJO phase speed and zonal wavenumber in the reference period of the RCP8.5. Note that these models that we have defined as good MJO models within the CMIP5 archive using these criteria differ from the models defined as good MJO models in other studies using different criteria (e.g., Jiang et al. 2015; Henderson et al. 2017; Bui and Maloney 2018) and provides a unique suite of models to examine the MJO's change in a warmer climate.

3. Changes in the characteristics of the MJO

a. Amplitude

Figure 3 shows the MJO amplitude (east power) against the west power in the RCP8.5 simulation. East power ranges from 0.92 to $1.57\,\mathrm{mm^2\,day^{-2}}$ in the reference period of RCP8.5, which is larger than the observed value ($\sim 0.53\,\mathrm{mm^2\,day^{-2}}$). East power in RCP8.5 shows a robust, linear increase in all models (colored symbols in Fig. 3), which is consistent with the results of previous studies (Subramanian et al. 2014; Schubert et al. 2013; Maloney and Xie 2013; Arnold et al. 2013, 2015; Adames et al. 2017a). The MJO amplification rate in the CMIP5 models ranges from 6.9% $\mathrm{K^{-1}}$ to 27.3% $\mathrm{K^{-1}}$. This broad range is likely due to the differences in the parameterization of moist physics among the models and differences in SST warming patterns (Takahashi et al. 2011; Maloney and Xie 2013; Bui and Maloney 2018).

The increase in MJO amplitude may not necessarily mean that a warmer climate is more favorable for MJO growth, but rather that the environment is more favorable for stronger convection in general, such that the MJO amplitude would increase without any unique changes to the growth or stability of the MJO. It is expected that the mean moisture and precipitation will increase as surface temperatures increase (Held and Soden 2006; Pendergrass and Hartmann 2014; Arnold et al. 2013). It was shown by Adames et al. (2017a,b) that fluctuations in moisture will rapidly increase with increasing CO_2. These increased fluctuations in moisture would also result in stronger precipitation variance. One would expect these fluctuations to enhance power across scales including those of the MJO even without any changes that are unique to the maintenance mechanism of the MJO. Adames et al. (2017b) also found a lengthening of the moisture residence time scale. The longer moisture residence time would cause the spatial and temporal scales of moisture to increase, which will in turn affect the spatial and temporal scales of precipitation.

Other studies have shown that the power spectrum of precipitation will become "redder" with warming (Arnold et al. 2013, 2015; Liu et al. 2013), which may be a result of longer-lasting precipitation events [larger lag-1 autocorrelation; Eq. (1) in Masunaga et al. 2006; Masunaga 2007; Gilman et al. 1963]. These longer-lasting events will project more strongly onto the largest temporal and spatial scales, meaning the spectral power in the low frequencies and low wavenumbers increases more rapidly than larger ones, and hence the redder spectrum. A redder spectrum implies stronger MJO activity, even without any changes in the stability of the MJO.

If the increase in MJO amplitude is simply due to an increase in the duration of precipitation, an increase in tropical precipitation variability may add power to both the westward-propagating waves and the MJO east power. This hypothesis can be verified by comparing the changes in east power with warming to that of west power (Fig. 3). The dashed lines in Fig. 3 indicate constant EWR values. While both east power and west power show a statistically significant increase over the twenty-first century under the RCP8.5 scenario, none of the models show notable changes in the EWR. This

Brought to you by NOAA Central Library | Unauthenticated | Downloaded 02/28/22 06:29 PM UTC

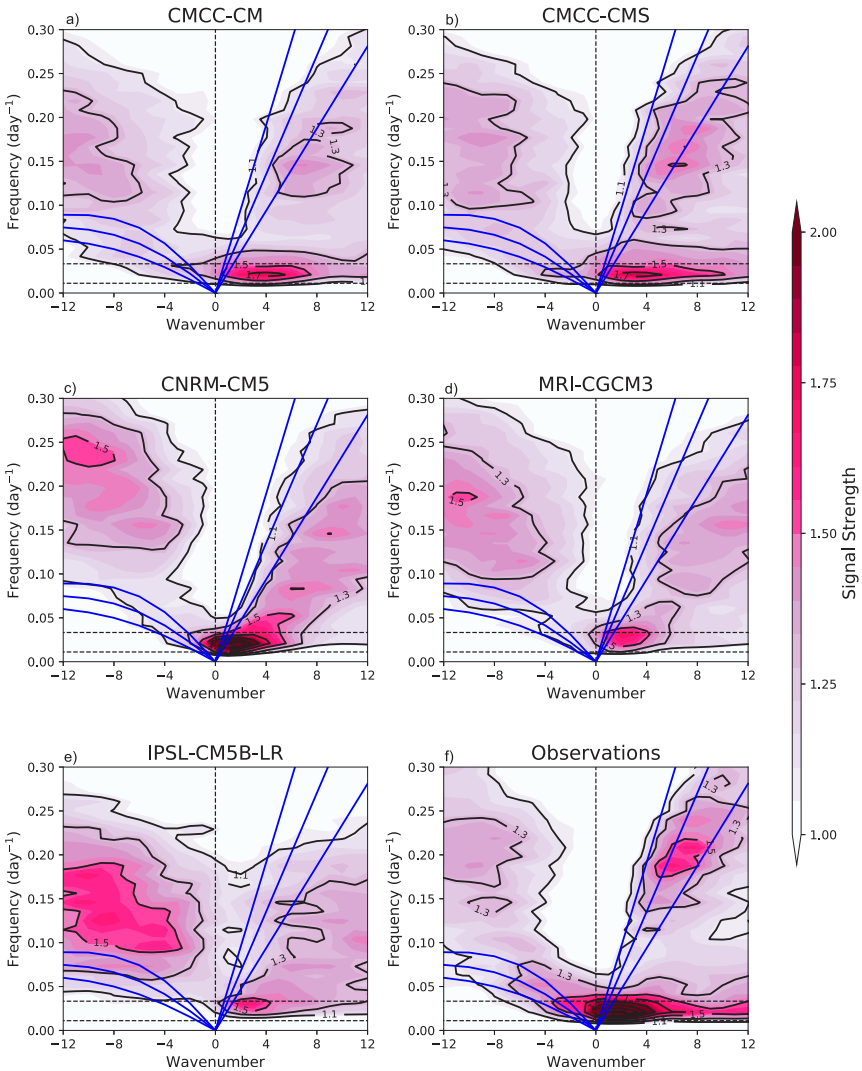

FIG. 1. Symmetric component of the normalized wavenumber–frequency power spectrum calculated following Wheeler and Kiladis (1999) for (a)–(e) the reference period of the RCP8.5 simulation of the CMIP5 models and (f) observations. Eastward-moving waves correspond to positive wavenumbers, while westward-moving waves correspond to negative wavenumbers. Blue lines represent the theoretical dispersion relation for equatorial Rossby waves (curved lines) and Kelvin waves (straight lines) for equivalent depths of 12, 25, and 50 m.

suggests that the same mechanism might be responsible for the increase in east power and west power. Figure 4 shows that while the increase in east power with warming is large and statistically significant (10.9% K^{-1}), the EWR shows a small weakening that is not statistically significant. Adames et al. (2017a) reported similar results using the simulations from the NASA GISS model. Pritchard and Yang (2016) also reported a similar result in SP-CAM, although their study considered SST changes and not changes in CO_2 concentrations. Some studies using individual models have found that the EWR increases with warming (Subramanian et al. 2014; Arnold et al. 2015). We find that while some of the CMIP5 models used in our study show an increase in the EWR (Fig. 4), there was no robust change found when the multimodel changes in EWR were examined.

b. *Phase speed and zonal scale*

Figure 5 shows the changes in MJO phase speed and zonal wavenumber in the RCP8.5 simulation. To elucidate these changes, we separate the RCP8.5 period into four 20-yr chunks (2021–40, 2041–60, 2061–80, 2081–2100) and analyze how the MJO changes in each of these periods. The shaded symbols in Fig. 5 represent each

Brought to you by NOAA Central Library | Unauthenticated | Downloaded 02/28/22 06:29 PM UTC

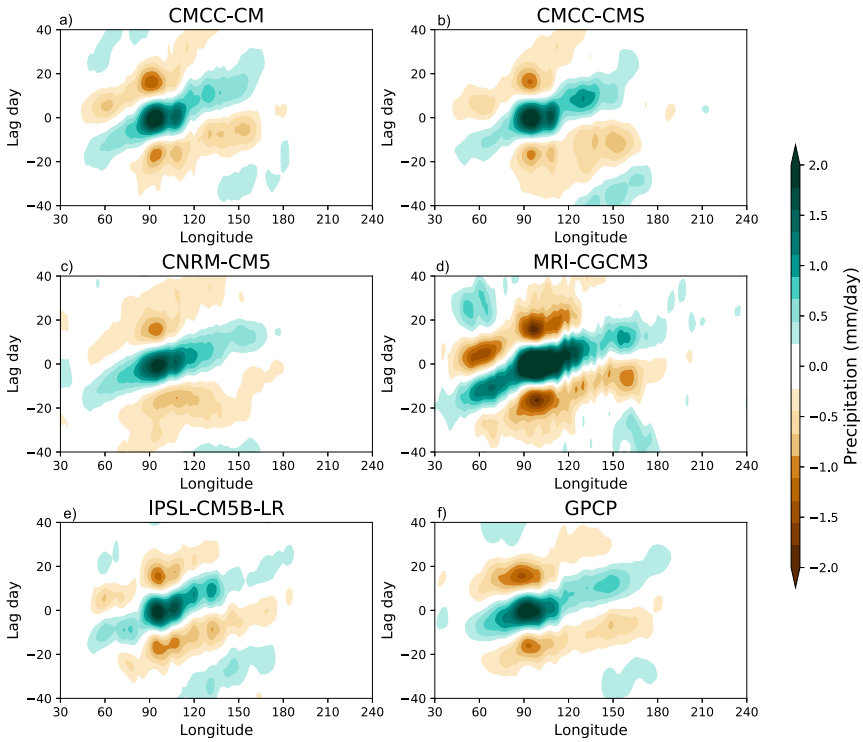

FIG. 2. Lag regression of 20–100-day bandpass-filtered precipitation anomalies in the (a)–(e) five CMIP5 models for reference period of RCP8.5 and (f) observations. The precipitation is averaged over 15°N–15°S and regressed onto precipitation averaged over the eastern Indian Ocean (90°–110°E). The magnitude of the shading is representative of the regression coefficient.

20-yr period in the RCP8.5 simulation. There is a systematic increase in the MJO phase speed and zonal scale, but the rate of change varies between models. CNRM-CM5 shows the largest increase in the phase speed with warming, while IPSL-CM5B-LR shows the largest changes in the zonal wavenumber.

The robust increase in the MJO phase speed in CMIP5 models is also consistent with the results of previous studies (Arnold et al. 2013, 2015; Chang et al. 2015; Adames et al. 2017a). The CMIP5 models compare well with the predicted increase in the MJO's phase speed in the NASA GISS model (Adames et al. 2017b), with the exception of CNRM-CM5. The increase in MJO zonal scale is also consistent with previous modeling studies that have examined these changes (Chang et al. 2015; Pritchard and Yang 2016; Adames et al. 2017a,b).

While there is insufficient evidence to affirm that the MJO maintenance mechanism changes with warming, the robust changes to the MJO phase speed indicate that the processes impacting MJO propagation experience changes with warming. In the following section, we examine these processes and how they influence the MJO's propagation.

4. Examining MJO phase speed changes using moisture mode theory

In this section, we employ the Adames and Kim (2016) moisture mode framework to understand the warming-induced MJO acceleration in the CMIP5 models. Our approach largely follows that of Adames et al. (2017b). Before presenting the results from the CMIP5 model simulations, we briefly summarize the aspects of moisture mode theory that are relevant to our study's examination of the eastward propagation of the MJO. Readers are referred to Adames and Kim (2016) and references therein for further details of the theory.

a. MJO's eastward propagation in the moisture mode theory

In the moisture mode theories, the evolution of convection is governed by that of column-integrated moisture or moist static energy. This approximation is based on the observed coupling between moisture and precipitation in the tropics (e.g., Bretherton et al. 2004; Holloway and Neelin 2009; Inoue and Back 2015; Ahmed and Schumacher 2015; Rushley et al. 2018). In this framework, the MJO's eastward propagation is the

Brought to you by NOAA Central Library | Unauthenticated | Downloaded 02/28/22 06:29 PM UTC

result of moistening to the east and drying to the west of enhanced moisture and convection. That is, for a given moisture perturbation (dashed line in Fig. 6), the rate of the moistening and drying (blue and brown circles in Fig. 6) determines the rate of eastward progression of the initial perturbation, that is, the phase speed of the moisture wave. Studies of the MJO's moisture or moist static energy budget in observations and in model simulations have shown that horizontal and vertical moisture advection are responsible for the moistening and drying (Benedict and Randall 2007; Andersen and Kuang 2012; Kim et al. 2014; Pritchard and Bretherton 2014; Adames and Wallace 2015; Wolding et al. 2016; Adames 2017; Jiang 2017; Adames et al. 2017b). Thus, MJO propagation is the result of interactions between moisture, diabatic heating, and circulation, as summarized in Fig. 6.

Positive moisture anomalies are associated with positive precipitation and therefore diabatic heating anomalies (moisture ↔ diabatic heating). In this relationship, the convective moisture adjustment time scale τ_c plays a central role by scaling the strength of the precipitation anomaly for a given moisture anomaly (e.g., Bretherton et al. 2004; Jiang et al. 2016; Rushley et al. 2018). The enhanced diabatic heating is primarily balanced by adiabatic cooling due to upward motion under the weak temperature gradient approximation (Charney 1963; Sobel et al. 2001). This upward motion drives horizontal circulation anomalies in the form of the Matsuno–Gill response (diabatic heating → circulation). Static stability S_p and zonal wavenumber k are the key parameters in this linkage, as static stability determines the magnitude of vertical motion required to balance a given diabatic heating while zonal wavenumber affects the magnitude of horizontal wind anomalies in the Matsuno–Gill response (Fig. 7). The zonal and meridional wind anomalies in the lower troposphere moisten (dry) the atmosphere to the east (west) through their impacts on advection of mean moisture, synoptic-scale eddy activity, and boundary layer convergence/divergence (circulation → moisture). The resulting moistening/drying results in the eastward propagation of the precipitation anomalies. The amount of moisture advection associated with the horizontal wind anomalies is set by the mean horizontal and vertical moisture gradients $\nabla\overline{\langle q\rangle}$ (where the brackets indicate mass-weighted vertical integration and the overline indicates the mean) because, for the same wind anomaly, a steeper moisture gradient would enhance moisture advection associated with it.

Moisture mode theory (Fig. 6) indicates that a set of parameters (τ_c, S_p, k, and $\nabla\overline{\langle q\rangle}$) control the magnitude of the moisture advection and thus the eastward propagation of the wave. For example, an increase in the mean moisture gradient would amplify the magnitude of moisture advection, accelerating the MJO. On the other hand, an increase in the convective moisture adjustment time scale, static stability, and zonal wavenumber would slow down the MJO by damping the moisture advection. These relationships between the key parameters and phase speed of the MJO are represented in Adames and Kim's (2016) dispersion relationship for the MJO:

$$c_{\mathrm{MJO}} = \frac{\tilde{p}A_{\mathrm{KR}}}{\tau_c k^2} \approx \frac{\tilde{p}\partial_y\overline{\langle q\rangle}}{2\tau_c\overline{M}_s k^2}, \tag{1}$$

where c_{MJO} is the phase speed of the MJO, $\tilde{p}$ is the weighting function for the dissipation of anomalous winds, A_{KR} is a parameter indicative of the magnitude of

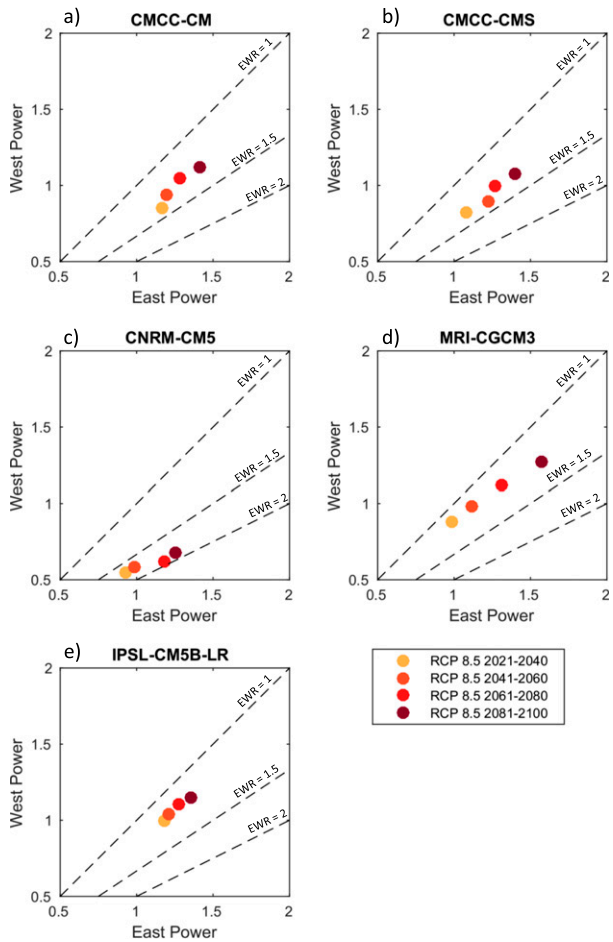

FIG. 3. Relationship between MJO power (east power) and the westward-propagating waves of the same size (west power) in the RCP8.5 simulation: (a) CMCC-CM, (b) CMCC-CMS, (c) CNRM-CM5, (d) MRI-CGCM3, and (e) IPSL-CM5B-LR. Colored symbols indicate different 20-yr periods of RCP8.5. Dashed lines indicate EWR = 1, 1.5, and 2.

Brought to you by NOAA Central Library | Unauthenticated | Downloaded 02/28/22 06:29 PM UTC

TABLE 1. List of models used in this study and their MJO phase speeds c_{MJO} and MJO zonal wavenumbers k. Observations from the GPCP precipitation (OBS) are included for comparison to the model values. The phase speed and zonal wavenumber are calculated for the reference period (2021–40) of the RCP8.5 simulation.

Model	c_{MJO} (m s^{-1})	k
CMCC-CM	5.50	3.20
CMCC-CMS	5.57	3.14
CNRM-CM5	6.08	2.74
MRI-CGCM3	5.82	3.09
IPSL-CM5B-LR	5.66	3.21
OBS	6.47	2.73

moisture advection by the combined Kelvin and Rossby wave components of the anomalous horizontal winds, τ_c is the convective moisture adjustment time scale, and k is the zonal wavenumber. Note that, in the original Adames and Kim (2016) dispersion relationship, the term A_{KR} takes into account changes to the total moisture advection by combining the effects of horizontal moisture advection, modulation of high-frequency eddy activity, surface heat fluxes, and frictional convergence. Following Adames et al. (2017b), we will approximate A_{KR} in Eq. (1) as the mean meridional moisture gradient $\partial_y\overline{\langle q\rangle}$ divided by 2 times the gross dry stability ($2\overline{M_s}$), which is a measure of the vertically integrated static stability. As shown in Fig. 9 of Adames et al. (2017b), this leads to an underestimation of the MJO phase speed, but it significantly simplifies our calculations. The zonal moisture gradient $\partial_x\overline{\langle q\rangle}$, while important for MJO propagation (Jiang 2017; Kim 2017; Kim et al. 2017), is not included here because the dispersion relation of Adames and Kim (2016) is linearized with respect to a zonally symmetric state. Additionally, the changes in the meridional moisture gradient with warming dominate the changes to the total moisture gradient with warming (not shown). The gross dry stability represents the static stability S_p felt by the first baroclinic mode in vertical motion. The gross dry stability is calculated by vertically integrating the vertical velocity–weighted vertical gradient of dry static energy s from the surface to 100 hPa:

$$\overline{M_s} = -\left\langle \Omega \frac{\partial \overline{s}}{\partial p} \right\rangle, \tag{2}$$

where $\overline{s}$ is the mean dry static energy and Ω is an idealized vertical velocity profile.

By differentiating Eq. (1) with respect to surface temperature T_s and dividing the result by Eq. (1), we obtain an expression for estimating the percentagewise changes in phase speed with warming:

$$\frac{\delta \ln c_{MJO}}{\delta T_s} \approx \frac{\delta \ln \partial_y \overline{\langle q\rangle}}{\delta T_s} - \frac{\delta \ln \overline{M_s}}{\delta T_s} - \frac{\delta \ln \tau_c}{\delta T_s} - \frac{2\delta \ln k}{\delta T_s}, \tag{3}$$

where changes in $\tilde{p}$ are small within the parameter range analyzed here (not shown) and therefore neglected, as in Adames et al. (2017b). If these relationships remain approximately exponential (linear when their natural logarithm is taken) in the range of our investigation, we can directly compare the percentagewise changes in the variables in Eq. (3) per kelvin of warming with our estimated changes in MJO phase speed. In the following subsections, we will examine the changes in these parameters

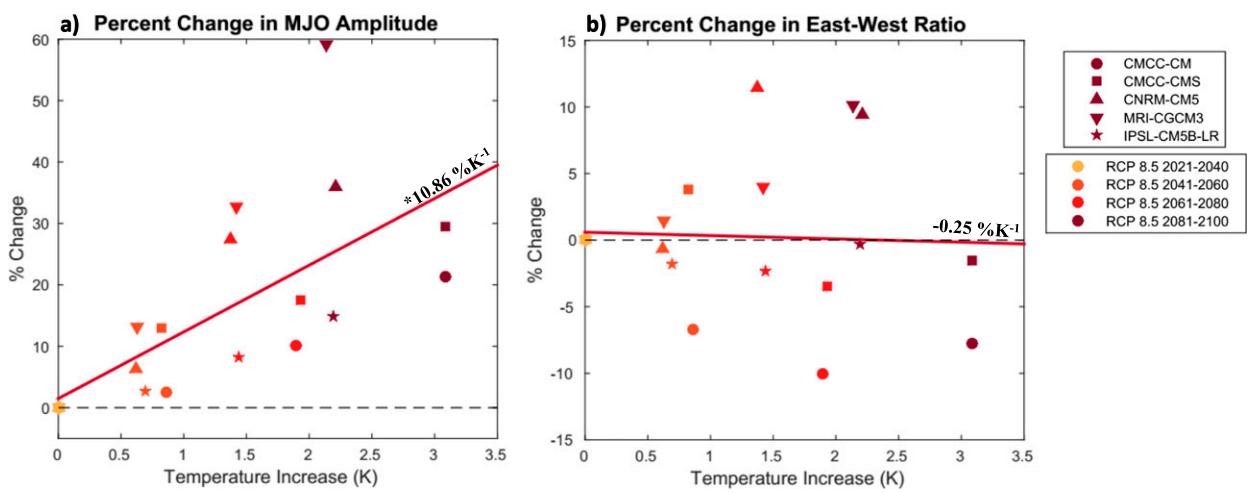

FIG. 4. (a) Percentage change in the MJO (east power) during 20-yr periods of RCP8.5 and (b) percentage change in the EWR during 20-yr periods of RCP8.5 with temperature. The shape of the symbols corresponds to the different CMIP5 models, while the color indicates the different 20-yr periods of RCP8.5. The red lines correspond to the multimodel fit of the (a) east power and (b) EWR, with the multimodel percentage change with temperature indicated on each line; the asterisk indicates a percentage change with temperature that is statistically significant.

Brought to you by NOAA Central Library | Unauthenticated | Downloaded 02/28/22 06:29 PM UTC

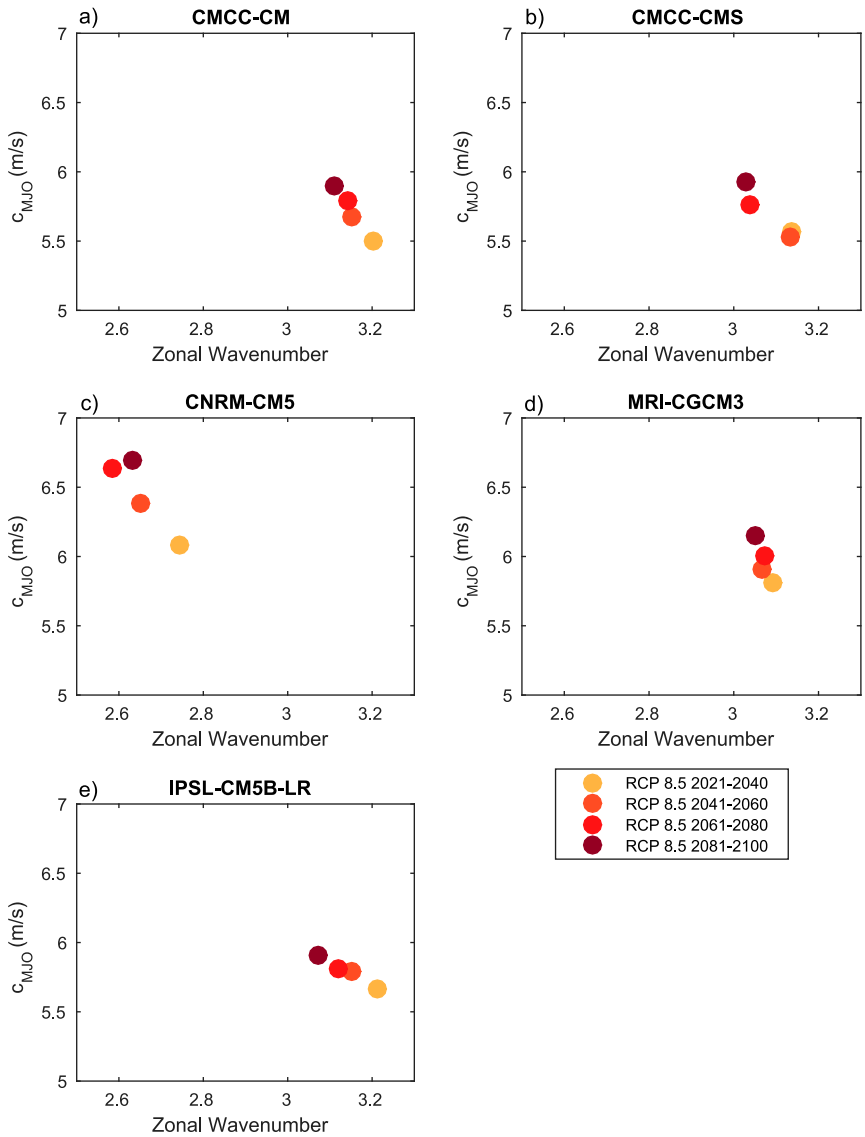

FIG. 5. Scatterplots of MJO's phase speed and zonal wavenumber in the RCP8.5 simulation: (a) CMCC-CM, (b) CMCC-CMS, (c) CNRM-CM5, (d) MRI-CGCM3, and (e) IPSL-CM5B-LR. Colors indicate different 20-yr periods of RCP8.5.

with warming in the CMIP5 models with a particular question in mind, Can we quantitatively explain the simulated MJO acceleration by the changes in the factors that are key to the moistening and drying rates?

b. Changes in the key parameters under the warming

This subsection examines the terms on the rhs of Eq. (3) in individual CMIP5 model simulations. The results will then be synthesized in section 5. To quantify the changes in the MJO due to greenhouse gas warming, we calculate the percentagewise changes between the latter three 20-yr periods of RCP8.5 and the reference period of RCP8.5 and fit a linear relationship to the percent changes with temperature. We use data within the same simulation to minimize the effect of other differences in the simulations (i.e., aerosol changes) on the mean state, allowing a closer comparison to the changes in the NASA GISS model with increasing CO_2.

1) MEAN MERIDIONAL MOISTURE GRADIENT

Under global warming, it is expected that moisture will increase more rapidly in the climatologically wet regions than in the dry regions of the tropics (Held and Soden 2006), causing a steepening of the mean meridional moisture gradients. The contours in Fig. 8 show the mean column-integrated specific humidity in the

Brought to you by NOAA Central Library | Unauthenticated | Downloaded 02/28/22 06:29 PM UTC

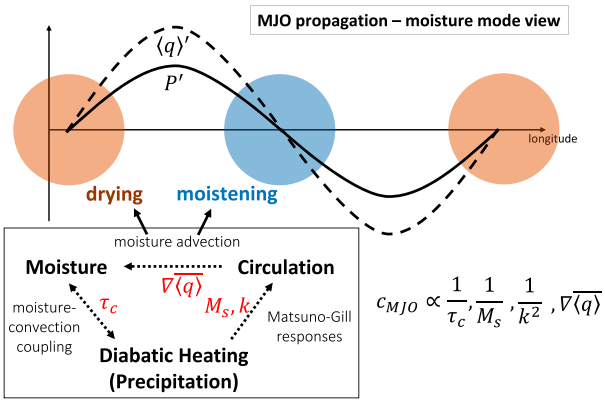

FIG. 6. Schematic of the MJO propagation in the moisture mode framework. The initial anomalies of precipitation P' (solid line) and moisture $\langle q \rangle'$ (dashed line) show a dipole of positive and negative anomalies. These anomalies lead to diabatic heating, which drives anomalous vertical and horizontal motions via the Matsuno–Gill responses. These circulation anomalies lead to moisture advection, which leads to drying (brown spots) and moistening (blue spots) to the west and east, respectively, of the precipitation anomaly. In the moisture mode framework, the magnitude of the moistening and drying by moisture advection is dependent on the horizontal moisture gradient $\nabla\overline{\langle q \rangle}$, the convective moisture adjustment time scale τ_c, gross dry stability M_s, and zonal wavenumber k of the initial moisture anomalies, and the phase speed c_{MJO} is proportional to $1/\tau_c$, $1/M_s$, $1/k^2$, and $\nabla\overline{\langle q \rangle}$ [see Eq. (1)].

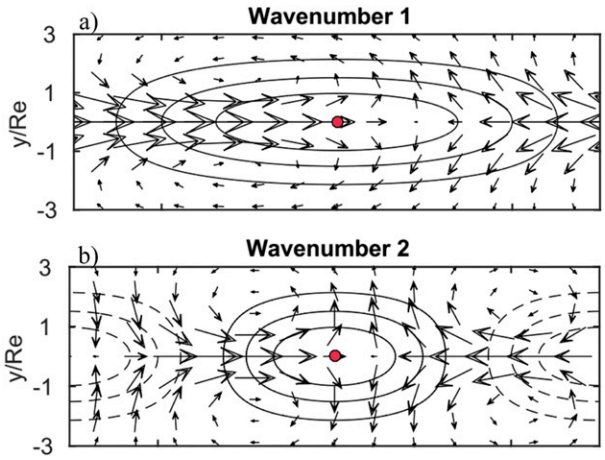

FIG. 7. The wind response to (a) a wavenumber-1 and (b) a wavenumber-2 heating anomaly (contours), plotted on a wavenumber-2 domain (half the radius of Earth). The latitudinal extent is the distance y normalized by the equatorial Rossby radius of deformation (Re). Vectors are anomalous horizontal winds; the maximum vector magnitude is 2.6 m s^{-1} for wavenumber 2 and 3.4 m s^{-1} for wavenumber 1. The anomalous horizontal winds are calculated using the Gill (1980) model.

reference period of RCP8.5. In all models, moisture is highest along the equator and over the Indo-Pacific warm pool. Figure 8 also shows the changes in the mean column-integrated specific humidity as the difference between the average over the last 20 years and the reference period of RCP8.5 (percentage changes for individual models are shown in Fig. 8). The changes in the CMIP5 models show larger increases in the deep tropics (peak near the equator between about 10°N and 10°S) than in the subtropics, indicating a clear steepening of the meridional moisture gradient. Both the climatological mean humidity pattern and its changes show a zonally elongated pattern, indicating that the changes in meridional gradient are dominant in the warm pool as the equatorial moisture increases and steepens the meridional gradient, while smoothing out the zonal gradient in this region.

To quantify the changes in the meridional moisture gradient, we calculate the absolute value of the meridional gradient of the time mean column moisture at each oceanic grid point, then average the mean meridional moisture gradient within the Indo-Pacific warm pool region (20°N–20°S, 60°–180°E). The column moisture is representative of the lower troposphere as it is weighted toward the lower troposphere and can be used to examine moisture transport over multiple levels. With the exception of MRI-CGCM3, the models show changes in the horizontal moisture gradient that are between 6% K^{-1} and 7% K^{-1}. MRI-CGCM3 has the lowest change in the moisture gradient with warming (4.3% K^{-1}), which is likely due to small changes over the majority of the Indo-Pacific warm pool (Fig. 8d). The steepening of the mean meridional moisture gradient would increase moisture advection for the same meridional wind anomaly, leading to larger moistening (drying) to the east (west) of the MJO heating anomaly. Assuming all other conditions remain constant, the enhanced moistening and drying to the east and west of the MJO heating anomaly would increase the MJO's phase speed [Eq. (3)].

2) GROSS DRY STABILITY

Under greenhouse gas–induced warming, the largest warming in the tropics occurs in the upper troposphere, which leads to increased static stability of the tropical atmosphere (Collins et al. 2013; Maloney and Xie 2013; Bony et al. 2006; Bui and Maloney 2018). For example, Bui and Maloney (2018) found an increase in the static stability in a different set of CMIP5 models and examined its role in the relationship between precipitation variability and low-level wind variability. Here, we focus on its implications on the magnitude of horizontal moisture advection. Figure 9 shows potential temperature changes in the tropics (30°S–30°N) between the reference period and the last 20 years of RCP8.5. All models show a warming pattern with the largest warming in the upper troposphere between 300 and 200 hPa, which is consistent with previous studies (Collins et al.

Brought to you by NOAA Central Library | Unauthenticated | Downloaded 02/28/22 06:29 PM UTC

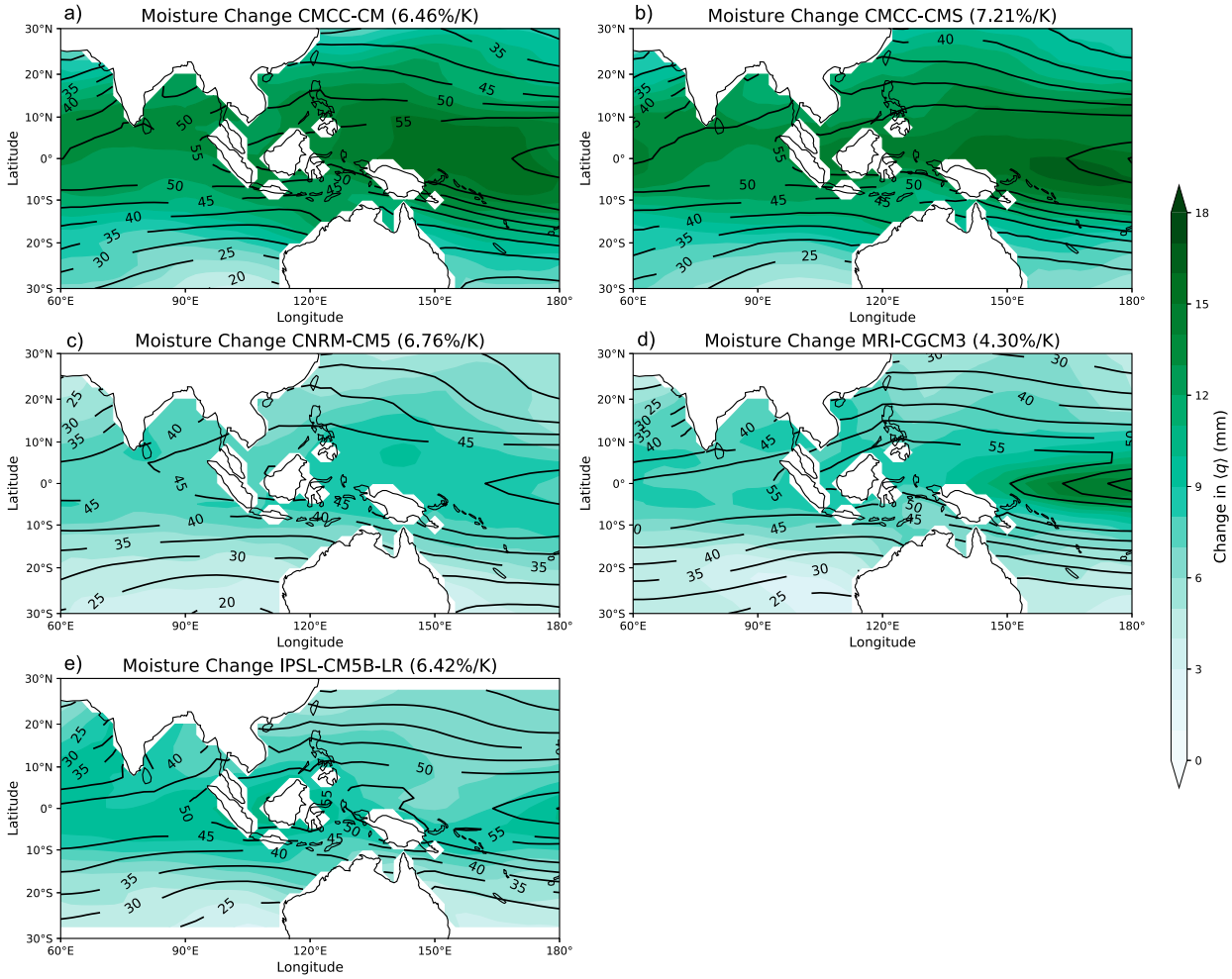

FIG. 8. The climatological mean column-integrated specific humidity for the reference period of RCP8.5 (contours) and the difference between the last 20 years of RCP8.5 and the reference period (shading): (a) CMCC-CM, (b) CMCC-CMS, (c) CNRM-CM5, (d) MRI-CGCM3, and (e) IPSL-CM5B-LR. The number in parentheses above each panel represents the percentage change of meridional moisture gradient per kelvin of warming over the Indo-Pacific warm pool for each model.

2013; Maloney and Xie 2013; Bony et al. 2006). Although CNRM-CM5, MRI-CGCM3, and IPSL-CM5B-LR have very similar changes in the lower troposphere, IPSL-CM5B-LR diverges from CNRM-CM5 and MRI-CGCM3 around 500 hPa and the upper-tropospheric warming is larger in IPSL-CM5B-LR than the other two models. CMCC-CM and CMCC-CMS are nearly parallel and exhibit larger warming throughout the troposphere than the other three models.

Results in Fig. 9 indicate that static stability increases with warming below around 200 hPa, which would act to slow down the MJO. We will estimate changes in the gross dry stability by using the approximation $\overline{s} \approx C_p\overline{\theta}$ (where C_p is the specific heat at constant pressure and θ is potential temperature). Additionally, we use the idealized Ω profile as defined by Adames and Kim (2016) for all models [see Eq. (A7) in Adames and Kim (2016)].

All models show an increase in the gross dry stability with warming (numbers next to model names in Fig. 9), with values ranging from 2.6% K^{-1} to 4.0% K^{-1}. CNRM-CM5, which shows the weakest warming in the upper troposphere, has the smallest rate of change in the gross dry stability. A more stable atmosphere implies that less vertical motion is required to offset diabatic heating and satisfy weak temperature gradient balance. With reduced vertical velocity anomalies, the divergent flow associated with deep convection will weaken. With weaker divergent flow, the vorticity generation from vortex stretching also weakens, resulting in a weaker nondivergent flow as well. Therefore, a stronger static stability will weaken the horizontal wind response and

Brought to you by NOAA Central Library | Unauthenticated | Downloaded 02/28/22 06:29 PM UTC

cause the advection of moisture by anomalous horizontal winds to decrease (Maloney and Xie 2013; Wolding et al. 2017; Bui and Maloney 2018). This will cause less moistening (drying) of the atmosphere to the east (west) of the MJO's heating anomaly, slowing the eastward propagation of the MJO [Eq. (3)].

3) Convective moisture adjustment time scale

The convective moisture adjustment time scale is a measure of the sensitivity of precipitation to moisture. It quantifies the hypothetical *e*-folding time scale of moisture anomalies under the assumption that only precipitation is affecting the moisture anomalies (Bretherton et al. 2004; Jiang et al. 2016; Rushley et al. 2018). We obtain the convective moisture adjustment time scale from the four 20-yr segments from RCP8.5 by calculating an exponential fit from the joint distribution of column relative humidity (CRH) and precipitation that describes the relationship between the two variables (Bretherton et al. 2004; Rushley et al. 2018; see Fig. 10 herein):

$$P = P_r \exp(a_d \mathrm{CRH}), \tag{5}$$

where P_r and a_d are coefficients of the nonlinear fit to each dataset. CRH is defined as

$$\mathrm{CRH} = \frac{\langle q \rangle}{\langle q_s \rangle}, \tag{6}$$

where $\langle q \rangle$ is the column-integrated specific humidity and $\langle q_s \rangle$ is the column-integrated saturation specific humidity. The convective moisture adjustment time scale is obtained from the inverse of the derivative of Eq. (5) evaluated at a reference CRH (CRH*):

$$\tau_c = \frac{\overline{\langle q_s \rangle}}{\partial P/\partial \mathrm{CRH}|_{\mathrm{CRH=CRH^*}}} = \frac{\overline{\langle q_s \rangle}}{P_r a_d \exp(a_d \mathrm{CRH^*})}, \tag{7}$$

where CRH* is defined as the value of CRH that corresponds to the mean precipitation over the near-equatorial area of the Indo-Pacific warm pool (10°S–10°N, 60°–180°E). Therefore, τ_c is affected by the shape of the exponential fit (P_r and a_d), the reference CRH value, and the climatological mean $\overline{\langle q_s \rangle}$. This method yields an estimated value of $\tau_c \approx 18$ h for SSM/I version 7 observations (Rushley et al. 2018), which is comparable to previous calculations (Bretherton et al. 2004; Sobel and Maloney 2012; Adames and Kim 2016).

Figure 10 shows the exponential fits of precipitation with CRH obtained from the four 20-yr periods of RCP8.5. (The corresponding joint histograms of moisture and precipitation are shown in Figs. S1–S5 in the online supplemental material.) The points in Fig. 10 indicate the value of the CRH* used in this study. In all models, precipitation rapidly increases with increasing CRH, as in observations. However, the shape of these curves varies significantly between models, implying large variations in τ_c as well (Rushley et al. 2018). CRH* is dependent on the change of the nonlinear relationship between moisture and precipitation and the change in the mean precipitation over the warm pool. An increase in CRH* in the CMIP5 models is primarily due to an increase in the mean precipitation, except for the CMCC-CM simulation in which the effect of the nonlinear fit is partially responsible for increasing CRH*. The fit in CMCC-CM becomes steeper with warming such that for the same mean precipitation, CRH* increases (Fig. 10a).

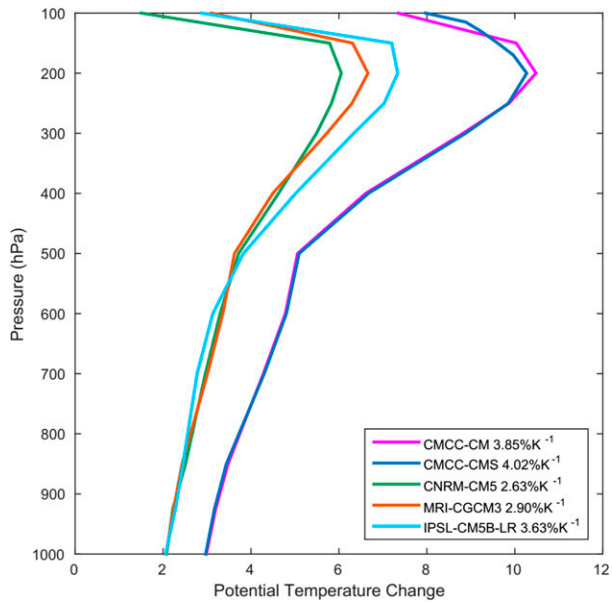

FIG. 9. Potential temperature difference from the last 20 years of RCP8.5 and the reference period for the CMIP5 models (colored lines). The numbers in the legend represent the percentage change in gross dry stability per kelvin for each model.

While the curve shows notable intermodel differences, its shape remains nearly unchanged throughout the RCP8.5 period in all models. This feature is most pronounced in IPSL-CM5B-LR, in which four curves from different simulation periods are nearly indistinguishable from each other. CMCC-CM shows the largest shift in the curve toward higher CRH at lower precipitation, while CMCC-CMS, CNRM-CM5, and MRI-CGCM3 show the largest changes in the curve at higher CRH and precipitation.

The wide range of changes in τ_c (percentage changes are noted in the lower-right corners in Fig. 10) indicates that the drivers of the changes in τ_c are not the same for each model. For instance, IPSL-CM5B-LR shows the largest changes in τ_c but the smallest change in CRH* and curve, indicating that changes to the curve and

Brought to you by NOAA Central Library | Unauthenticated | Downloaded 02/28/22 06:29 PM UTC

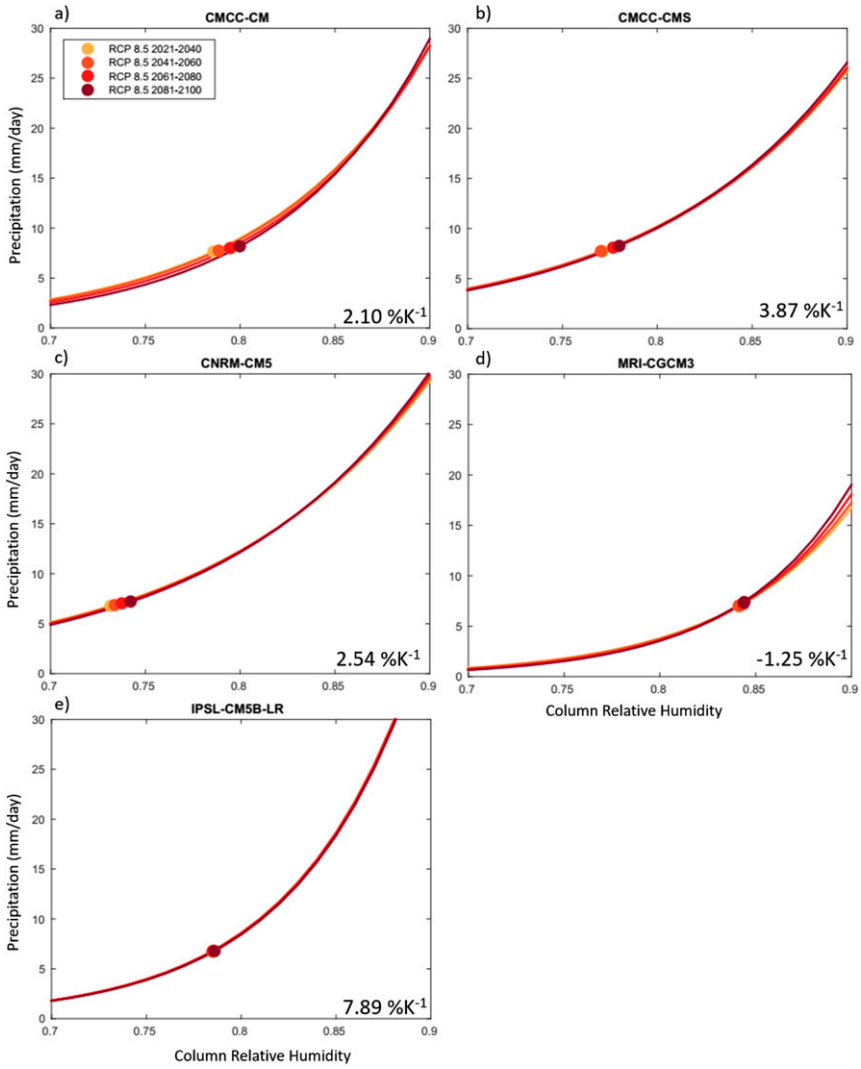

FIG. 10. The nonlinear moisture–precipitation relationship for the CMIP5 models: (a) CMCC-CM, (b) CMCC-CMS, (c) CNRM-CM5, (d) MRI-CGCM3, and (e) IPSL-CM5B-LR. Colored symbols indicate the reference CRH for the different 20-yr periods of RCP8.5. The reference CRH corresponds to the mean precipitation of the Indo-Pacific warm pool. The colored lines show the different relationship between CRH and precipitation in the different 20-yr periods of RCP8.5 (colors correspond to the color of the reference CRH). Percentage change of each model with surface warming is shown in the bottom-right corner of each panel.

CRH* are not enough to explain the large changes to τ_c. CMCC-CM, CMCC-CMS, and CNRM-CM5 show a more modest increase in τ_c and larger changes in CRH*. While it is reasonable to expect that an increase in CRH* would decrease τ_c, the change in CRH* is offset by large changes in $\overline{\langle q_s \rangle}$, which consistently increases during the RCP8.5 warming scenario. In CMCC-CM, CMCC-CMS, CNRM-CM5, and IPSL-CM5B-LR, the changes in $\overline{\langle q_s \rangle}$ outpace that of the denominator of Eq. (7), leading to an increase in τ_c. This result is consistent with the findings of Adames et al. (2017b). In the case of IPSL-CM5B-LR, the small changes in CRH* lead to larger changes in τ_c as the changes are not offset by large changes in CRH*.

An interesting outlier is MRI-CGCM3, which is the only model to show a decrease in τ_c ($-1.2\%\ \mathrm{K}^{-1}$). The joint histogram of this model (Fig. S4) shows a significantly higher number of values near CRH = 1 than the other models. Vertical profiles of q and q_s (not shown) indicate that this model has very high moisture in the mid- to upper atmosphere, which is exhibited by the high number of values at high CRH. MRI-CGCM3 is the only model in which the denominator of Eq. (7) outpaces changes in $\overline{\langle q_s \rangle}$, leading to a decrease in τ_c.

Brought to you by NOAA Central Library | Unauthenticated | Downloaded 02/28/22 06:29 PM UTC

In four out of five models, τ_c increases with warming, indicating that convection becomes less sensitive to moisture in a warmer climate. This suggests that for the same value of column-integrated specific humidity, a longer τ_c would lead to a lower precipitation anomaly P' and hence a weaker diabatic heating anomaly Q'. A decrease in Q' will be balanced by a decreased anomalous vertical velocity, which will weaken the anomalous horizontal wind response and therefore moisture advection, slowing the MJO. The rate of increase in τ_c varies significantly from model to model, ranging from an increase of 2.1% K^{-1} to 7.9% K^{-1} (excluding MRI-CGCM3). The intermodel spread (despite the limited ensemble size) may originate from the uncertainty in the parameterized moist physics in GCMs, which was also found in Rushley et al. (2018).

4) Zonal wavenumber

The CMIP5 models simulate a robust decrease in the MJO's zonal wavenumber with warming (Fig. 5). The changes in the zonal wavenumber range from −0.5% K^{-1} to −1.9% K^{-1}. While the mechanism behind the widening of the MJO's zonal scale remains unclear, it has important implications for the phase speed of the MJO in the Adames and Kim (2016) moisture mode framework. That is, a larger MJO zonal scale will result in faster MJO propagation. This is partly because larger waves will have a greater wind response than smaller waves with the same heating anomaly (Fig. 7), which is a characteristic of the Matsuno–Gill solution and represented in the fourth term in the rhs of Eq. (3).

5. Explaining MJO phase speed changes

In this section, we summarize the results presented in the previous section and seek to explain changes to the MJO phase speed by synthesizing the changes in each term on the rhs of Eq. (3). The multimodel mean change in the MJO's actual phase speed with warming is ~2.4% K^{-1} (Fig. 11a). The phase speed has a strong linear relationship with warming, with a small amount of intermodel spread. The increase in the meridional moisture gradient over the warm pool region (Fig. 11b) has a magnitude of ~6.6% K^{-1}, which compares well with the expected increase in moisture with warming based on the Clausius–Clapeyron relationship (Held and Soden 2006). The meridional moisture gradient explains most of the increase in the moisture gradient in the CMIP5 models (Fig. 8). The gross dry stability and the convective moisture adjustment time scale increase at a rate of ~3.7% K^{-1} (Fig. 11c) and ~3.1% K^{-1} (Fig. 11d), respectively. In Fig. 11e, we see that there is a decrease in the zonal wavenumber of ~1.4% K^{-1}. All of the changes to these variables show a linear relationship with surface temperature changes, with varying spread among models.

According to Eq. (3) and the simulated changes, the changes in the humidity gradient and wavenumber act to speed up the MJO, while the changes in the gross dry stability and the convective moisture adjustment time scale act to slow it down. The percentage changes of these terms and the predicted and calculated phase speed are summarized in Table 2. The sum of the change in the rhs of Eq. (3) indicates that the predicted acceleration in MJO propagation is comparable with the calculated changes for most models and multimodel changes, with some models overestimating the phase speed changes and others underestimating the changes. This indicates that the framework described by Adames and Kim (2016) works well for examining changes to the MJO phase speed. The IPSL-CM5B-LR changes show that from the rhs of Eq. (3), a decrease in the MJO phase speed would be expected, which is contradictory to the calculated acceleration of the MJO with warming. This is likely due to the anomalously large changes in the convective moisture adjustment time scale in this model.

These changes may be dependent on the model physics, particularly on the convection schemes of these models as evidenced by the varying moisture–precipitation relationships (Fig. 10). IPSL-CM5B-LR shows a high sensitivity of precipitation to moisture, leading to a dearth in high CRH as the precipitation rapidly removes moisture from the column (Fig. S5). Conversely, MRI-CGCM3 has an extremely moist atmosphere (Fig. S4), leading to low sensitivity of precipitation to moisture, allowing the atmosphere to get very moist before rain occurs. The moisture–precipitation relationship in these models does not accurately represent the moisture–precipitation relationship in observations (Rushley et al. 2018). As discussed in section 4a, the tight coupling of moisture and precipitation in the tropics is a fundamental relationship for the moisture mode theory. The variety of relationships seen in these models speaks to the variety of convection schemes in the CMIP5 models and brings to light potential limitations in calculating changes to the MJO phase speed in models with differing moisture–precipitation relationships.

6. Summary and conclusions

This study uses five CMIP5 models to examine changes to the MJO magnitude and phase speed under greenhouse gas–induced warming. Models were selected based on their superior ability to accurately represent the MJO. The percent changes in MJO amplitude and west power in the four 20-yr periods of the RCP8.5 simulation relative to the reference period are examined. The expected

Brought to you by NOAA Central Library | Unauthenticated | Downloaded 02/28/22 06:29 PM UTC

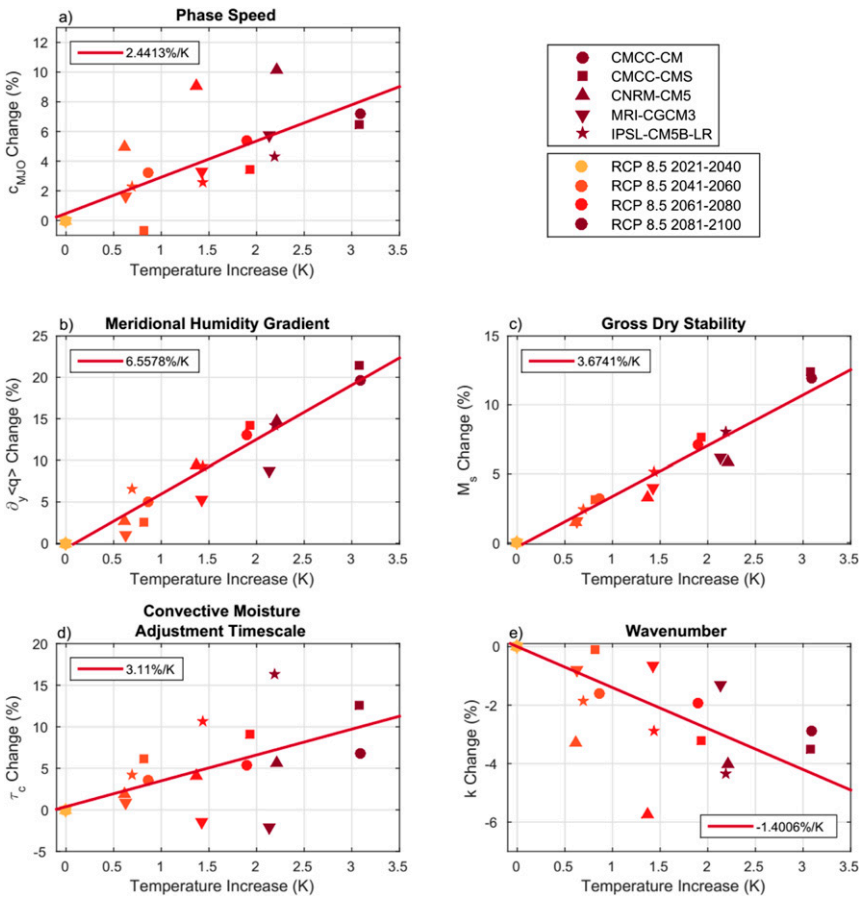

FIG. 11. Percentage changes with respect to the reference period (a) phase speed, (b) humidity gradient, (c) gross dry stability, (d) convective moisture adjustment time scale, and (e) wavenumber with the amount of surface temperature increase. The colors correspond to the 20-yr periods of RCP8.5 simulation, while symbol shapes correspond to the different CMIP5 model. The lines are the linear best fit for the percentage changes with temperature over all of the models. Magnitudes of these fits (i.e., the multimodel mean changes) are in the upper-left (lower right in the case of the zonal wavenumber) corner of each panel.

changes in the MJO phase speed over the RCP8.5 scenario are compared to the calculated MJO phase speed in the models following the linear moisture mode framework of Adames and Kim (2016).

Our study reveals that the MJO amplitude increases with warming in all models, supporting results from previous studies (Subramanian et al. 2014; Schubert et al. 2013; Maloney and Xie 2013; Arnold et al. 2013, 2015; Wolding et al. 2017; Adames et al. 2017a). The amplitude of westward-traveling waves of the same temporal and spatial scales as the MJO increase at a similar rate, resulting in an EWR that remains nearly unchanged throughout the RCP8.5 period in all models. This result indicates that the amplification of the MJO and west power may be due to the overall increase in background tropical precipitation. Though some models agree with previous studies that show an increase in the EWR (Subramanian et al. 2014; Arnold et al. 2015), there is no robust response in the sign of the EWR changes in the CMIP5 models. Such an amplification suggests that the growth mechanism for the MJO is not strongly affected by greenhouse gas–induced warming. Adames et al. (2017b) found a similar result in the NASA GISS model.

The MJO phase speed increases with increasing temperature in all five CMIP5 models, which is also consistent with previous studies (Slingo et al. 1999; Arnold et al. 2013, 2015; Chang et al. 2015; Adames et al. 2017a). By using the linear moisture mode framework of Adames and Kim (2016) with respect to surface temperature, we attempted to quantitatively explain changes to the MJO phase speed. It is found that the simulated MJO acceleration can be explained by the changes in the mean meridional humidity gradient, gross dry stability, convective moisture adjustment time scale, and MJO zonal

Brought to you by NOAA Central Library | Unauthenticated | Downloaded 02/28/22 06:29 PM UTC

TABLE 2. Percentage changes per kelvin of surface warming for phase speed calculated from the models $[\delta\ln(c_{\mathrm{MJO}})/\delta T_s]_a$ and phase speed predicted by Eq. (3) $[\delta\ln(c_{\mathrm{MJO}})/\delta T_s]_p$. The predicted value is the sum of the percentage changes of the meridional humidity gradient ($\delta\ln\partial_y\langle\overline{q}\rangle/\delta T_s$), gross dry stability ($-\delta\ln\overline{M_s}/\delta T_s$), convective moisture adjustment time scale ($-\delta\ln\tau_c/\delta T_s$), and zonal wavenumber ($-2\delta\ln k/\delta T_s$). The first row shows the multimodel mean changes, and subsequent rows are the results for the individual models.

Model	$\left[\frac{\delta\ln(c_{\mathrm{MJO}})}{\delta T_s}\right]_a$	$\left[\frac{\delta\ln(c_{\mathrm{MJO}})}{\delta T_s}\right]_p$	$\frac{\delta\ln\partial_y\langle\overline{q}\rangle}{\delta T_s}$	$-\frac{\delta\ln\overline{M_s}}{\delta T_s}$	$-\frac{\delta\ln\tau_c}{\delta T_s}$	$-\frac{2\delta\ln k}{\delta T_s}$
All models	2.44	2.55	6.56	−3.67	−3.14	2.80
CMCC-CM	2.27	2.24	6.47	−3.85	−2.10	1.72
CMCC-CMS	2.33	2.15	7.39	−4.02	−3.87	2.65
CNRM-CM5	4.56	5.49	6.95	−2.63	−2.54	3.71
MRI-CGCM3	2.62	3.65	4.29	−2.90	1.24	1.02
IPSL-CM5B-LR	1.80	−1.03	6.67	−3.63	−7.89	3.82

wavenumber, which determine the rate of moistening and drying around MJO moisture anomalies. The gross dry stability and moisture gradient exhibit an increase with warming, as expected from previous studies (Maloney and Xie 2013; Chang et al. 2015; Collins et al. 2013; Held and Soden 2006; Adames et al. 2017b). With the exception of MRI-GCGM3, the convective moisture adjustment time scale also increases in the CMIP5 models.

The multimodel mean shows that changes to the key parameters and MJO zonal wavenumber in CMIP5 models can explain changes in the phase speed. The changes in the gross dry stability and convective moisture adjustment time scale slow down the MJO propagation, while the changes in the mean moisture gradient and MJO zonal wavenumber lead to an increase in the MJO phase speed. The latter two variables dominate the changes to the MJO phase speed in the CMIP5 models, leading to an increase in the phase speed of the MJO. Thus, our results suggest that the moisture mode framework and the Adames and Kim (2016) framework can adequately explain how the MJO responds to increasing CO_2, at least from the point of view of a multimodel ensemble.

The phase speed increase with warming in the CMIP5 models has a similar rate to the NASA GISS model, which shows an increase at a rate of ~3.3% K^{-1} (Adames et al. 2017a). The models agree with the NASA GISS model meridional moisture gradient change (~6.9% K^{-1}). Changes in MRI-CGCM3 are much smaller than the other CMIP5 models, which shows comparatively small changes along the equatorial warm pool (Fig. 8). The gross dry stability in the CMIP5 models increases at a similar magnitude to the NASA GISS model (~4.0% K^{-1}). The NASA GISS model's convective moisture adjustment time scale increases at a rate of ~5% K^{-1} (Adames et al. 2017b), which is larger than the increase in all of the models considered here, except IPSL-CM5B-LR. Last, the changes in the MJO zonal wavenumber are generally smaller than those found in the NASA GISS model (−2.8% K^{-1}; Adames et al. 2017a).

The convective moisture adjustment time scale can be altered by overall changes in the moisture–precipitation relationship as well as changes to the mean precipitation (which changes the reference CRH) or changes in the mean saturation specific humidity. The increase in the convective moisture adjustment time scale seen in the models can be attributed to large changes in $\overline{\langle q_s\rangle}$, in agreement with Adames et al. (2107b). The changes associated with the moisture–precipitation relationship may also be affected by the changes to the stability of the atmosphere and the horizontal advection of moisture, which can act to suppress or drive convection. It would be of interest to examine in closer detail the physical driver of changes to the nonlinear moisture–precipitation relationship.

The MJO zonal wavenumber is another interesting component of this study, as its changes, in part, drive the MJO phase speed changes, but it may also be influenced by the mean state. For instance, changes in the static stability of the atmosphere or mean moisture gradients can alter the horizontal scale of moisture and heating anomalies that would modulate the scale of the MJO. There is currently no clear mechanism that could explain why the MJO increases in scale with warming. Future research may shed some light onto how the MJO scale is selected and how greenhouse gas–induced warming affects this scale.

Acknowledgments. The authors thank Eric Maloney and three anonymous reviewers for their helpful comments. SSM/I and SSMIS data are produced by Remote Sensing Systems and are available online (www.remss.com/missions/ssmi). CMIP5 model simulations are available at the CMIP5 archive. SSR and DK were supported by the National Aeronautics and Space Administration Grant 80NSSC17K0227 and by Korean Meteorological Administration Research and Development Program under Grant KMI2018-03110. DK was also supported by the U.S. Department of Energy's Regional and Global Model Analysis program under the

Brought to you by NOAA Central Library | Unauthenticated | Downloaded 02/28/22 06:29 PM UTC

Grant Number DE-SC0016223. AFA was supported by the National Oceanic and Atmospheric Administration (NOAA) Grant NA15OAR4310099 and by the University of Michigan's startup package.

REFERENCES

Adames, Á. F., 2017: Precipitation budget of the Madden–Julian oscillation. *J. Atmos. Sci.*, **74**, 1799–1817, https://doi.org/10.1175/JAS-D-16-0242.1.

——, and J. M. Wallace, 2015: Three-dimensional structure and evolution of the moisture field in the MJO. *J. Atmos. Sci.*, **72**, 3733–3754, https://doi.org/10.1175/JAS-D-15-0003.1.

——, and D. Kim, 2016: The MJO as a dispersive, convectively coupled moisture wave: Theory and observations. *J. Atmos. Sci.*, **73**, 913–941, https://doi.org/10.1175/JAS-D-15-0170.1; Corrigendum, **74**, 3121–3124, https://doi.org/10.1175/JAS-D-17-0071.1.

——, ——, A. H. Sobel, A. D. Genio, and J. Wu, 2017a: Changes in the structure and propagation of the MJO with increasing CO_2. *J. Adv. Model. Earth Syst.*, **9**, 1251–1268, https://doi.org/10.1002/2017MS000913.

——, ——, ——, ——, and ——, 2017b: Characterization of moist processes associated with changes in the propagation of MJO with increasing CO_2. *J. Adv. Model. Earth Syst.*, **9**, 2946–2967, https://doi.org/10.1002/2017MS001040.

Ahmed, F., and C. Schumacher, 2015: Convective and stratiform components of the precipitation-moisture relationship. *Geophys. Res. Lett.*, **42**, 10 453–10 462, https://doi.org/10.1002/2015GL066957.

Andersen, J. A., and Z. Kuang, 2012: Moist static energy budget of MJO-like disturbances in the atmosphere of a zonally symmetric aquaplanet. *J. Climate*, **25**, 2782–2804, https://doi.org/10.1175/JCLI-D-11-00168.1.

Arnold, N. P., Z. Kuang, and E. Tziperman, 2013: Enhanced MJO-like variability at high SST. *J. Climate*, **26**, 988–1001, https://doi.org/10.1175/JCLI-D-12-00272.1.

——, M. Branson, Z. Kuang, D. A. Randall, and E. Tziperman, 2015: MJO intensification with warming in the superparameterized CESM. *J. Climate*, **28**, 2706–2724, https://doi.org/10.1175/JCLI-D-14-00494.1.

Benedict, J. J., and D. A. Randall, 2007: Observed characteristics of the MJO relative to maximum rainfall. *J. Atmos. Sci.*, **64**, 2332–2354, https://doi.org/10.1175/JAS3968.1.

Bony, S., and Coauthors, 2006: How well do we understand and evaluate climate change feedback processes? *J. Climate*, **19**, 3445–3482, https://doi.org/10.1175/JCLI3819.1.

Bretherton, C. S., M. E. Peters, and L. E. Back, 2004: Relationships between water vapor path and precipitation over the tropical oceans. *J. Climate*, **17**, 1517–1528, https://doi.org/10.1175/1520-0442(2004)017<1517:RBWVPA>2.0.CO;2.

Bui, H. X., and E. D. Maloney, 2018: Change in the Madden-Julian oscillation precipitation and wind variance under global warming. *Geophys. Res. Lett.*, **45**, 7148–7155, https://doi.org/10.1029/2018GL078504.

Cassou, C., 2008: Intraseasonal interaction between the Madden-Julian oscillation and the North Atlantic Oscillation. *Nature*, **455**, 523–527, https://doi.org/10.1038/nature07286.

Chang, C.-W. J., W.-L. Tseng, H.-H. Hsu, N. Keenlyside, and B.-J. Tsuang, 2015: The Madden-Julian oscillation in a warmer world. *Geophys. Res. Lett.*, **42**, 6034–6042, https://doi.org/10.1002/2015GL065095.

Charney, J. G., 1963: A note on large-scale motions in the tropics. *J. Atmos. Sci.*, **20**, 607–609, https://doi.org/10.1175/1520-0469(1963)020<0607:ANOLSM>2.0.CO;2.

Collins, M., and Coauthors, 2013: Long-term climate change: Projections, commitments, and irreversibility. *Climate Change 2013: The Physical Science Basis*, T. F. Stocker et al., Eds., Cambridge University Press, 1029–1136, https://www.ipcc.ch/site/assets/uploads/2018/02/WG1AR5_Chapter12_FINAL.pdf.

Dee, D. P., and Coauthors, 2011: The ERA-Interim reanalysis: Configuration and performance of the data assimilation system. *Quart. J. Roy. Meteor. Soc.*, **137**, 553–597, https://doi.org/10.1002/qj.828.

Fuchs, Z., and D. J. Raymond, 2005: Large-scale modes in a rotating atmosphere with radiative-convective instability and WISHE. *J. Atmos. Sci.*, **62**, 4084–4094, https://doi.org/10.1175/JAS3582.1.

——, and ——, 2007: A simple, vertically resolved model of tropical disturbances with a humidity closure. *Tellus*, **59A**, 344–354, https://doi.org/10.1111/j.1600-0870.2007.00230.x.

Gill, A. E., 1980: Some simple solutions for heat-induced tropical circulation. *Quart. J. Roy. Meteor. Soc.*, **106**, 447–462, https://doi.org/10.1002/qj.49710644905.

Gilman, D. L., F. J. Fuglister, and J. M. Mitchell Jr., 1963: On the power spectrum of "red noise." *J. Atmos. Sci.*, **20**, 182–184, https://doi.org/10.1175/1520-0469(1963)020<0182:OTPSON>2.0.CO;2.

Haertel, P., 2018: Sensitivity of the Madden Julian oscillation to ocean warming in a Lagrangian atmospheric model. *Climate*, **6**, 45, https://doi.org/10.3390/cli6020045.

——, K. Straub, and A. Budsock, 2015: Transforming circumnavigating Kelvin waves that initiate and dissipate the Madden–Julian oscillation. *Quart. J. Roy. Meteor. Soc.*, **141**, 1586–1602, https://doi.org/10.1002/qj.2461.

Hayashi, Y., 1971: A generalized method of resolving disturbances into progressive and retrogressive waves by space Fourier and time cross-spectral analyses. *J. Meteor. Soc. Japan*, **49**, 125–128, https://doi.org/10.2151/jmsj1965.49.2_125.

Held, I. M., and B. J. Soden, 2006: Robust responses of the hydrological cycle to global warming. *J. Climate*, **19**, 5686–5699, https://doi.org/10.1175/JCLI3990.1; Corrigendum, **24**, 1559–1560, https://doi.org/10.1175/2010JCLI4045.1.

Henderson, S. A., E. D. Maloney, and S.-W. Son, 2017: Madden–Julian oscillation Pacific teleconnections: The impact of the basic state and MJO representation in general circulation models. *J. Climate*, **30**, 4567–4586, https://doi.org/10.1175/JCLI-D-16-0789.1.

Hendon, H. H., C. Zhang, and J. D. Glick, 1999: Interannual variation of the Madden–Julian oscillation during austral summer. *J. Climate*, **12**, 2538–2550, https://doi.org/10.1175/1520-0442(1999)012<2538:IVOTMJ>2.0.CO;2.

Hilburn, K. A., and F. J. Wentz, 2008: Intercalibrated passive microwave rain products from the unified microwave ocean retrieval algorithm. *J. Appl. Meteor. Climatol.*, **47**, 778–795, https://doi.org/10.1175/2007JAMC1635.1.

Holloway, C. E., and J. D. Neelin, 2009: Moisture vertical structure, column water vapor, and tropical deep convection. *J. Atmos. Sci.*, **66**, 1665–1683, https://doi.org/10.1175/2008JAS2806.1.

Huffman, G. J., R. F. Adler, M. M. Morrissey, D. T. Bolvin, S. Curtis, R. Joyce, B. McGavock, and J. Susskind, 2001: Global precipitation at one-degree daily resolution from multisatellite observations. *J. Hydrometeor.*, **2**, 36–50, https://doi.org/10.1175/1525-7541(2001)002<0036:GPAODD>2.0.CO;2.

Inoue, K., and L. E. Back, 2015: Gross moist stability assessment during TOGA COARE: Various interpretations of gross

Brought to you by NOAA Central Library | Unauthenticated | Downloaded 02/28/22 06:29 PM UTC

moist stability. *J. Atmos. Sci.*, **72**, 4148–4166, https://doi.org/10.1175/JAS-D-15-0092.1.

Jiang, X., 2017: Key processes for the eastward propagation of the Madden-Julian oscillation based on multimodel simulations. *J. Geophys. Res. Atmos.*, **122**, 755–770, https://doi.org/10.1002/2016JD025955.

——, and Coauthors, 2015: Vertical structure and physical processes of the Madden-Julian oscillation: Exploring key model physics in climate simulations. *J. Geophys. Res. Atmos.*, **120**, 4718–4748, https://doi.org/10.1002/2014JD022375.

——, M. Zhao, E. D. Maloney, and D. E. Waliser, 2016: Convective moisture adjustment time scale as a key factor in regulating model amplitude of the Madden-Julian oscillation. *Geophys. Res. Lett.*, **43**, 10 412–10 419, https://doi.org/10.1002/2016GL070898.

Kerns, B. W., and S. S. Chen, 2016: Large-scale precipitation tracking and the MJO over the Maritime Continent and Indo-Pacific warm pool. *J. Geophys. Res. Atmos.*, **121**, 8755–8776, https://doi.org/10.1002/2015JD024661.

Kim, B.-M., G.-H. Lim, and K.-Y. Kim, 2006: A new look at the midlatitude-MJO teleconnection in the Northern Hemisphere winter. *Quart. J. Roy. Meteor. Soc.*, **132**, 485–503, https://doi.org/10.1256/qj.04.87.

Kim, D., J.-S. Kug, and A. H. Sobel, 2014: Propagating versus nonpropagating Madden–Julian oscillation events. *J. Climate*, **27**, 111–125, https://doi.org/10.1175/JCLI-D-13-00084.1.

——, H. Kim, and M.-I. Lee, 2017: Why does the MJO detour the Maritime Continent during austral summer? *Geophys. Res. Lett.*, **44**, 2579–2587, https://doi.org/10.1002/2017GL072643.

Kim, H.-M., 2017: The impact of the mean moisture bias on the key physics of MJO propagation in the ECMWF reforecast. *J. Geophys. Res. Atmos.*, **122**, 7772–7784, https://doi.org/10.1002/2017JD027005.

Lin, J.-L., and Coauthors, 2006: Tropical intraseasonal variability in 14 IPCC AR4 climate models. Part I: Convective signals. *J. Climate*, **19**, 2665–2690, https://doi.org/10.1175/JCLI3735.1.

Liu, P., T. Li, B. Wang, M. Zhang, J.-J. Luo, Y. Masumoto, X. Wang, and E. Roeckner, 2013: MJO change with A1B global warming estimated by the 40-km ECHAM5. *Climate Dyn.*, **41**, 1009–1023, https://doi.org/10.1007/s00382-012-1532-8.

Madden, R. A., and P. R. Julian, 1972: Description of global-scale circulation cells in the tropics with a 40–50 day period. *J. Atmos. Sci.*, **29**, 1109–1123, https://doi.org/10.1175/1520-0469(1972)029<1109:DOGSCC>2.0.CO;2.

Maloney, E. D., and D. L. Hartmann, 2000a: Modulation of eastern North Pacific hurricanes by the Madden–Julian oscillation. *J. Climate*, **13**, 1451–1460, https://doi.org/10.1175/1520-0442(2000)013<1451:MOENPH>2.0.CO;2.

——, and ——, 2000b: Modulation of hurricane activity in the Gulf of Mexico by the Madden-Julian oscillation. *Science*, **287**, 2002–2004, https://doi.org/10.1126/science.287.5460.2002.

——, and S.-P. Xie, 2013: Sensitivity of tropical intraseasonal variability to the pattern of climate warming. *J. Adv. Model. Earth Syst.*, **5**, 32–47, https://doi.org/10.1029/2012MS000171.

——, A. H. Sobel, and W. M. Hannah, 2010: Intraseasonal variability in an aquaplanet general circulation model. *J. Adv. Model. Earth Syst.*, **2**, 5, https://doi.org/10.3894/JAMES.2010.2.5.

Marshall, A. G., and H. H. Hendon, 2015: Subseasonal predication of the Australian summer monsoon anomalies. *Geophys. Res. Lett.*, **42**, 10 913–10 919, https://doi.org/10.1002/2015GL067086.

——, O. Alves, and H. H. Hendon, 2009: A coupled GCM analysis of MJO activity at the onset of El Niño. *J. Atmos. Sci.*, **66**, 966–983, https://doi.org/10.1175/2008JAS2855.1.

Masunaga, H., 2007: Seasonality and regionality of the Madden–Julian oscillation, Kelvin wave, and equatorial Rossby wave. *J. Atmos. Sci.*, **64**, 4400–4416, https://doi.org/10.1175/2007JAS2179.1.

——, T. S. L'Ecuyer, and C. D. Kummerow, 2006: The Madden–Julian oscillation recorded in early observations from the Tropical Rainfall Measuring Mission (TRMM). *J. Atmos. Sci.*, **63**, 2777–2794, https://doi.org/10.1175/JAS3783.1.

Matsuno, T., 1966: Quasi-geostrophic motions in the equatorial area. *J. Meteor. Soc. Japan*, **44**, 25–42, https://doi.org/10.2151/jmsj1965.44.1_25.

Matthews, A. J., 2000: Propagation mechanisms for the Madden–Julian oscillation. *Quart. J. Roy. Meteor. Soc.*, **126**, 2637–2651, https://doi.org/10.1002/qj.49712656902.

——, 2008: Primary and successive events in the Madden–Julian oscillation. *Quart. J. Roy. Meteor. Soc.*, **134**, 439–453, https://doi.org/10.1002/qj.224.

Milliff, R. F., and R. A. Madden, 1996: The existence and vertical structure of fast, eastward-moving disturbances in the equatorial troposphere. *J. Atmos. Sci.*, **53**, 586–597, https://doi.org/10.1175/1520-0469(1996)053<0586:TEAVSO>2.0.CO;2.

Pendergrass, A. G., and D. L. Hartmann, 2014: The atmospheric energy constraint on global-mean precipitation change. *J. Climate*, **27**, 757–768, https://doi.org/10.1175/JCLI-D-13-00163.1.

Pohl, B., and A. J. Matthew, 2007: Observed changes in the lifetime and amplitude of the Madden–Julian oscillation associated with interannual ENSO sea surface temperature anomalies. *J. Climate*, **20**, 2659–2674, https://doi.org/10.1175/JCLI4230.1.

Powell, S. W., and R. A. Houze Jr., 2015: Effect of dry large-scale vertical motion on initial MJO convective onset. *J. Geophys. Res. Atmos.*, **120**, 4783–4805, https://doi.org/10.1002/2014JD022961.

Pritchard, M. S., and C. S. Bretherton, 2014: Causal evidence that rotational moisture advection is critical to the superparameterized Madden–Julian oscillation. *J. Atmos. Sci.*, **71**, 800–815, https://doi.org/10.1175/JAS-D-13-0119.1.

——, and D. Yang, 2016: Response of the superparameterized Madden–Julian oscillation to extreme climate and basic state variation challenges a moisture mode view. *J. Climate*, **29**, 4995–5008, https://doi.org/10.1175/JCLI-D-15-0790.1.

Raymond, D. J., and Z. Fuchs, 2009: Moisture modes and the Madden–Julian oscillation. *J. Climate*, **22**, 3031–3046, https://doi.org/10.1175/2008JCLI2739.1.

Risbey, J. S., M. J. Pook, P. C. McIntosh, M. C. Wheeler, and H. H. Hendon, 2009: On the remote drivers of rainfall variability in Australia. *Mon. Wea. Rev.*, **137**, 3233–3253, https://doi.org/10.1175/2009MWR2861.1.

Rushley, S. S., D. Kim, C. S. Bretherton, and M.-S. Ahn, 2018: Reexamining the nonlinear moisture-precipitation relationship over the tropical oceans. *Geophys. Res. Lett.*, **45**, 1133–1140, https://doi.org/10.1002/2017GL076296.

Schubert, J. J., B. Stevens, and T. Crueger, 2013: Madden-Julian oscillation as simulated by the MPI Earth System Model: Over the last and into the next millennium. *J. Adv. Model. Earth Syst.*, **5**, 71–84, https://doi.org/10.1029/2012MS000180.

Slingo, J. M., D. P. Rowell, K. R. Sperber, and F. Nortley, 1999: On the predictability of the interannual behavior of the Madden-Julian oscillation and its relationship with El Niño. *Quart. J. Roy. Meteor. Sci.*, **125**, 583–609, https://doi.org/10.1002/qj.49712555411.

Sobel, A., and E. Maloney, 2012: An idealized semi-empirical framework for modeling the Madden–Julian oscillation. *J. Atmos. Sci.*, **69**, 1691–1705, https://doi.org/10.1175/JAS-D-11-0118.1.

Brought to you by NOAA Central Library | Unauthenticated | Downloaded 02/28/22 06:29 PM UTC

——, and ——, 2013: Moisture modes and the eastward propagation of the MJO. *J. Atmos. Sci.*, **70**, 187–192, https://doi.org/10.1175/JAS-D-12-0189.1.

——, J. Nilsson, and L. M. Polvani, 2001: The weak temperature gradient approximation and balanced tropical moisture waves. *J. Atmos. Sci.*, **58**, 3650–3665, https://doi.org/10.1175/1520-0469(2001)058<3650:TWTGAA>2.0.CO;2.

Subramanian, A., M. Jochum, A. J. Miller, R. Neale, H. Seo, D. Waliser, and R. Murtugudde, 2014: The MJO and global warming: A study in CCSM4. *Climate Dyn.*, **42**, 2019–2031, https://doi.org/10.1007/s00382-013-1846-1.

Sugiyama, M., 2009: The moisture mode in the quasi-equilibrium tropical circulation model. Part I: Analysis based on the weak temperature gradient approximation. *J. Atmos. Sci.*, **66**, 1507–1523, https://doi.org/10.1175/2008JAS2690.1.

Takahashi, C., N. Sato, A. Seiki, K. Yoneyama, and R. Shirooka, 2011: Projected future change of MJO and its extratropical teleconnection in East Asia during the northern winter simulated in IPCC AR4 models. *SOLA*, **7**, 201–204, https://doi.org/10.2151/sola.2011-051.

Taylor, K. E., R. J. Stouffer, and G. A. Meehl, 2012: An overview of CMIP5 and the experiment design. *Bull. Amer. Meteor. Soc.*, **93**, 485–498, https://doi.org/10.1175/BAMS-D-11-00094.1.

Wentz, F. J., K. A. Hilburn, and D. K. Smith, 2012: Remote Sensing Systems DMSP SSM/I daily environmental suite on 0.25° grid, version 7. Remote Sensing Systems, accessed 25 June 2017, Santa Rosa, CA, www.remss.com/missions/ssmi.

Wheeler, M., and G. N. Kiladis, 1999: Convectively coupled equatorial waves: Analysis of clouds and temperature in the wavenumber–frequency domain. *J. Atmos. Sci.*, **56**, 374–399, https://doi.org/10.1175/1520-0469(1999)056<0374:CCEWAO>2.0.CO;2.

——, H. H. Hendon, S. Cleland, H. Meinke, and A. Donald, 2009: Impacts of the Madden–Julian oscillation on the Australian rainfall and circulation. *J. Climate*, **22**, 1482–1498, https://doi.org/10.1175/2008JCLI2595.1.

Wolding, B. O., and E. D. Maloney, 2015: Objective diagnostics and the Madden–Julian oscillation. Part II: Application to moist static energy and moisture budgets. *J. Climate*, **28**, 7786–7808, https://doi.org/10.1175/JCLI-D-14-00689.1.

——, ——, and M. Branson, 2016: Vertically resolved weak temperature gradient analysis of the Madden-Julian oscillation in SP-CESM. *J. Adv. Model. Earth Syst.*, **8**, 1586–1619, https://doi.org/10.1002/2016MS000724.

——, ——, S. Henderson, and M. Branson, 2017: Climate change and the Madden-Julian oscillation: A vertically resolved weak temperature gradient analysis. *J. Adv. Model. Earth Syst.*, **9**, 307–331, https://doi.org/10.1002/2016MS000843.

Zhang, C., 2013: Madden–Julian oscillation: Bridging weather and climate. *Bull. Amer. Meteor. Soc.*, **94**, 1849–1870, https://doi.org/10.1175/BAMS-D-12-00026.1.

——, and J. Ling, 2017: Barrier effect of the Indo-Pacific Maritime Continent on the MJO: Perspectives from tracking MJO precipitation. *J. Climate*, **30**, 3439–3459, https://doi.org/10.1175/JCLI-D-16-0614.1.

Brought to you by NOAA Central Library | Unauthenticated | Downloaded 02/28/22 06:29 PM UTC